Spectral embedding based active contour (SEAC) for lesion segmentation on breast dynamic contrast enhanced magnetic resonance imaging

Shannon C. Agner[a)]
Department of Biomedical Engineering, Rutgers University, Piscataway, New Jersey 08854

Jun Xu
School of Information and Control, Nanjing University of Information Science and Technology, Nanjing 210044, China

Anant Madabhushi[b)]
Department of Biomedical Engineering, Case Western Reserve University, Cleveland, Ohio 44106

(Received 4 March 2012; revised 16 September 2012; accepted for publication 17 September 2012; published 28 February 2013)

Purpose: Segmentation of breast lesions on dynamic contrast enhanced (DCE) magnetic resonance imaging (MRI) is the first step in lesion diagnosis in a computer-aided diagnosis framework. Because manual segmentation of such lesions is both time consuming and highly susceptible to human error and issues of reproducibility, an automated lesion segmentation method is highly desirable. Traditional automated image segmentation methods such as boundary-based active contour (AC) models require a strong gradient at the lesion boundary. Even when region-based terms are introduced to an AC model, grayscale image intensities often do not allow for clear definition of foreground and background region statistics. Thus, there is a need to find alternative image representations that might provide (1) strong gradients at the margin of the object of interest (OOI); and (2) larger separation between intensity distributions and region statistics for the foreground and background, which are necessary to halt evolution of the AC model upon reaching the border of the OOI.

Methods: In this paper, the authors introduce a spectral embedding (SE) based AC (SEAC) for lesion segmentation on breast DCE-MRI. SE, a nonlinear dimensionality reduction scheme, is applied to the DCE time series in a voxelwise fashion to reduce several time point images to a single parametric image where every voxel is characterized by the three dominant eigenvectors. This parametric eigenvector image (PrEIm) representation allows for better capture of image region statistics and stronger gradients for use with a hybrid AC model, which is driven by both boundary and region information. They compare SEAC to ACs that employ fuzzy c-means (FCM) and principal component analysis (PCA) as alternative image representations. Segmentation performance was evaluated by boundary and region metrics as well as comparing lesion classification using morphological features from SEAC, PCA+AC, and FCM+AC.

Results: On a cohort of 50 breast DCE-MRI studies, PrEIm yielded overall better region and boundary-based statistics compared to the original DCE-MR image, FCM, and PCA based image representations. Additionally, SEAC outperformed a hybrid AC applied to both PCA and FCM image representations. Mean dice similarity coefficient (DSC) for SEAC was significantly better (DSC $= 0.74 \pm 0.21$) than FCM+AC (DSC $= 0.50 \pm 0.32$) and similar to PCA+AC (DSC $= 0.73 \pm 0.22$). Boundary-based metrics of mean absolute difference and Hausdorff distance followed the same trends. Of the automated segmentation methods, breast lesion classification based on morphologic features derived from SEAC segmentation using a support vector machine classifier also performed better (AUC $= 0.67 \pm 0.05$; $p < 0.05$) than FCM+AC (AUC $= 0.50 \pm 0.07$), and PCA+AC (AUC $= 0.49 \pm 0.07$).

Conclusions: In this work, we presented SEAC, an accurate, general purpose AC segmentation tool that could be applied to any imaging domain that employs time series data. SE allows for projection of time series data into a PrEIm representation so that every voxel is characterized by the dominant eigenvectors, capturing the global and local time-intensity curve similarities in the data. This PrEIm allows for the calculation of strong tensor gradients and better region statistics than the original image intensities or alternative image representations such as PCA and FCM. The PrEIm also allows for building a more accurate hybrid AC scheme. © *2013 American Association of Physicists in Medicine*. [http://dx.doi.org/10.1118/1.4790466]

Key words: computer aided diagnosis, breast cancer, segmentation, active contour, spectral embedding, classification, DCE-MRI

I. BACKGROUND

Breast lesion segmentation is an important preprocessing step in a computer aided diagnosis (CAD) framework for breast dynamic contrast enhanced (DCE) magnetic resonance imaging (MRI). Several studies have shown that quantitative morphological features extracted from breast lesions are helpful for distinguishing between benign and malignant breast lesions.[1,2] Typically, a radiologist's expert delineation of the lesion boundary is considered the gold standard for lesion segmentation. However, manual segmentation is notoriously susceptible to inter-rater variability in breast MRI interpretation[1,3] and is extremely time consuming. For these reasons, automated methods for lesion segmentation are warranted.

Because accurate lesion segmentation is time consuming, many groups have explored various automated segmentation methods for breast DCE-MRI.[4–8] Automated lesion segmentation methods for breast DCE-MRI have been explored mostly in the context of voxelwise clustering of the data. Szabo *et al.*[4] used a voxelwise classifier that used dynamic contrast signal intensities in conjunction with an artificial neural network to identify lesion areas of interest. Other researchers who have also used voxelwise classifiers for segmentation include Twellmann *et al.*,[5] who used the dynamic contrast signal intensities in conjunction with a support vector machine (SVM) classifier and Chen *et al.*,[6] who used a fuzzy c-means (FCM) clustering scheme. Additionally, Wu *et al.*[7] clustered the time-series data of breast DCE-MRI using Markov random fields. Although these voxelwise methods are reasonably effective, most require postprocessing morphological operations such as hole-filling and dilation in order to provide a closed contour for the lesion of interest.

An alternative to voxelwise methods are shape-based deformable models, most popular of which is the active contour (AC) (Refs. 9–15) model. The theory of the AC, introduced by Kass *et al.*,[9] is that (1) the segmentation of any object of interest (OOI) in an image, whose edges can be described by a closed curve, is equivalent to the location of edges, or sharp intensity gradients; and (2) this segmentation can be generated by iteratively deforming a curve toward the edges of the OOI. Traditional AC models have been typically classified as: (1) boundary based,[9,10] such as the AC described by Kass *et al.*,[9] or (2) region-based methods.[11] However, to use an AC model, an image representation that is conducive to the stopping criteria of the curve evolution is necessary. For example, boundary-based methods require strong gradients located at the boundary of the OOI to provide an effective stopping criterion for the evolving AC model. For radiologic imaging applications involving MRI or computed tomography (CT) data, boundary-based methods may not be effective due to image acquisition artifacts such as partial volume effects[16,17] and a low signal to noise ratio. These may result in fuzziness of the object boundary, thus reducing the effectiveness of the stopping criteria. Region-based methods rely on the image statistics of foreground and background regions in the image. A grayscale radiologic image may not provide a large enough difference between foreground and background image statistics to provide an effective stopping criterion for a region-based AC. Consequently, AC methods require the use of alternative image representations that might provide (1) strong gradients at the margin of the OOI; and (2) larger separation between intensity distributions and region statistics for the foreground and the background which would allow the AC to stop evolving at the border of the OOI.

Alternative image representations have been previously explored for noise filtering,[18] image registration,[19] and fuzzy connectedness-based image segmentation.[20] Nyul *et al.*[19] employed ball-scale for multiprotocol image registration, where ball-scale[19] is a locally adaptive scale definition such that every image voxel location is parametrized by the radius of the largest ball that satisfies some predefined local homogeneity criterion. Saha[21] defined tensor scale (*t*-scale) at every spatial location as the largest ellipse that satisfies some predefined homogeneity criterion at that location. The *t*-scale based representation has been employed in the context of image segmentation and filtering.[21,22] A generalized scale representation introduced by Madabhushi and Udupa[23] was applied similar to bias field correction,[23] noise filtering,[24] and intensity standardization.[25] For each of these local scale notions, transforming the data into an alternative image space allowed for an improvement in the corresponding image processing tasks.

Nonlinear dimensionality reduction (NLDR) methods attempt to transform data from a high-dimensional space to a more manageable, low-dimensional space representation and can be particularly powerful in data visualization[26] and classification.[27–29] Spectral embedding (SE), a type of NLDR, uses the eigenvectors corresponding to the minimum eigenvalues derived from the eigenvalue decomposition of a weighted affinity matrix,[30] where the affinity matrix represents the pairwise dissimilarity between all the objects to be classified, obtained via a Gaussian, exponential, or polynomial kernel in the original feature space. SE also allows for parametrically representing high-dimensional data in a reduced dimensional space, and several researchers have employed SE in the context of image partitioning[30,31] and clustering.[32] The primary hypothesis driving the work presented in this paper is that the application of SE to time series or longitudinal data might allow for better capture and representation of both region and boundary-based statistics compared to currently available methods. In addition, these improved region and boundary statistics can allow for construction of improved hybrid active contour schemes. To the best of our knowledge, no attempts have been made thus far to explore the utility of NLDR schemes to seek improved image representations that would be amenable for use in conjunction with an AC-based segmentation scheme.

II. PREVIOUS RELATED WORK AND MOTIVATION

The traditional AC operates on the scalar grayscale image intensities. However, time series data, such as DCE-MRI, contain multiple time points over which the image of the lesion of interest is captured. Typically, if a traditional AC

is used, only a single time point (usually the time point at which the lesion maximally enhances) is used for segmentation. However, implementations of the AC model have been developed for multidimensional images.[12–15] Chan *et al.*[13] presented an extension of the original scalar image-based AC model applied to vector-valued images. Rousson and Deriche[14] also presented a vector-valued active contour. In a recent application to a medical imaging problem, Xu *et al.*[15] developed a tensor gradient-based AC for use with histopathological images by computing the gradient from vectorial images. Xu *et al.*[15] showed that the tensor gradient more completely captured the gradient information in a multichannel image than using a single channel of the image, yielding a more accurate AC scheme.

SE aims to partition the data instances in a way that maximizes intracluster similarity while simultaneously minimizing intercluster similarity,[30] and the eigenvectors are oriented along the directions of fundamental patterns in the data. In the context of DCE-MRI, these fundamental patterns are related to the time-intensity curves at each voxel in the image, and the time-intensity curves from lesion and nonlesion areas tend to have different characteristics as previously shown in multiple different studies.[4,6] Thus, by applying SE across all voxels in an image, we are able to characterize voxels according to their time-intensity curves, an approach that, to our knowledge, has not been taken before with respect to DCE-MRI data. In addition, voxel similarity is reflected by the eigenvectors at each voxel such that voxels with similar eigenvector values have similar time-intensity curves. Because this is performed in a voxelwise fashion, the image scene composed of the eigenvector values reflect region similarities and global differences in the images (see Fig. 1).

Using this alternative image scene information driven by the intensity profiles can provide greater knowledge for approximating the region statistics of the image via SE's ability to preserve global data information.[30] Similarly, the alternative image scene information resulting from SE provides better boundary information by preserving the local image information as well as constraining the data in such a way that the distances between voxel clusters with different time-intensity curve profiles will be maximized.

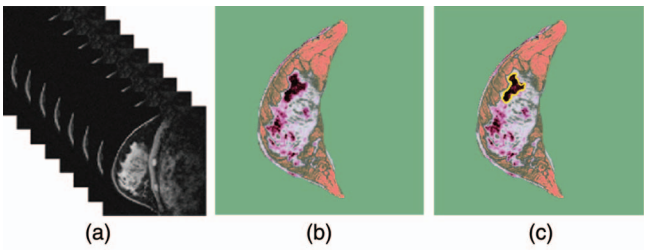

FIG. 1. Workflow of SEAC. (a) Each time point image for a given MR slice is collated, and every voxel location is characterized by a T-dimensional signal intensity vector, where T represents the total number of time points at which the MRI is acquired during the course of the administration of the contrast agent. (b) SE is performed in a voxelwise fashion to preserve global and local similarities in time-intensity curves at each voxel, where voxels having similar colors signify similar time-intensity curves. (c) A hybrid AC segmentation, manually initialized in the vicinity of the lesion, leverages the improved region and boundary-based statistics to generate a final lesion segmentation (shown via the yellow curve).

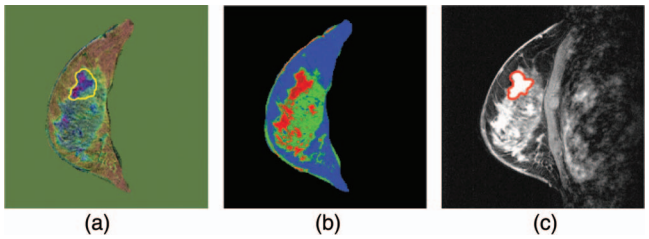

FIG. 2. (a) PCA is used as an alternative image representation (Ref. 27) to drive the AC and is unable to successfully stop at the lesion boundary because the image gradients at the lesion boundary are not strong enough (final segmentation as yellow curve). (b) FCM is unable to capture the lesion at all using the AC, and no contour results. (c) Ground truth manual segmentation by a radiologist who is blinded to lesion diagnosis is shown in red superimposed on the maximum contrast enhancement image.

Recently, Eyal *et al.*[27] used the principal eigenvectors derived from principal component analysis (PCA) to determine a parametric representation of breast DCE-MRI data for lesion classification. In contrast to SE, the feature matrix in PCA is a covariance matrix. The eigenvectors associated with the largest eigenvalues rotate the data along axes of maximum variance, and if used in the context of a boundary-based AC, the gradient functional derived from the PCA eigenvectors would be based on a gradient of deviation from the mean. Image gradients derived in this fashion may not be strong enough in some cases to serve as the stopping criterion for an AC formulation, which is illustrated by the example in Fig. 2(a), where the AC overshoots the boundary of the OOI unlike the SEAC model in Fig. 1(c).

In this paper, we present a new SE-based AC (SEAC) scheme for segmentation of lesions on time series data such as DCE-MRI. SEAC results in strong gradients at object boundaries. SE can be applied to any multidimensional, longitudinal, or time-series data whereby the multiattribute data are reduced to a single parametric image representation, though in this work we have limited our application to breast DCE-MRI. Each voxel in this reduced dimensional, parametric image representation is characterized by the set of orthonormal eigenvectors that aim to preserve both local and global similarities,[30] so a SE approach might also yield improved region-based statistics, which in conjunction with stronger boundary gradients results in an improved hybrid AC scheme. We compare SEAC to alternative image representation methods which use (1) the original grayscale image at peak contrast enhancement (peakCE) to drive the AC (peakCE+AC); (2) FCM to drive the AC (FCM+AC); and (3) principal components derived from PCA to drive the AC segmentation (PCA+AC). SEAC is quantitatively compared to peakCE+AC, FCM+AC, and PCA+AC by calculating both boundary- and region-based metrics which compare the final segmentation resulting from SEAC, peakCE+AC, PCA+AC, and FCM+AC to the ground truth segmentation performed manually by a radiologist who is blinded to the lesion diagnosis. The accuracy of SEAC is further compared to FCM+AC,[6,8] the method widely used for automated breast

lesion segmentation on DCE-MRI, as well as PCA+AC by comparing the classification accuracy. In this case, classification accuracy is based on quantitative morphology features of the lesions which are extracted from the automated segmentation (SEAC, PCA+AC, or FCM+AC) methods. The use of SEAC is not limited to DCE-MRI data alone and could potentially be used for lesion detection and segmentation on other types of longitudinal or time series data as well as other types of multiparametric imaging (e.g., T1-, T2-, and diffusion-weighted imaging).

The remainder of the paper is as follows. Section III contains a brief overview of the SEAC algorithm and theory. Section IV describes the calculation of the gradient tensors derived from SE. Section V describes the hybrid AC used in conjunction with SE. Section VI comprises the experimental design. Section VII describes the results and discussion, and in Section VIII we present concluding remarks.

III. BRIEF OVERVIEW OF SEAC

This section provides an introduction to the workflow for SEAC, illustrated in Fig. 1.

Step 1. Apply SE to the DCE-MRI: Let $\mathcal{F} = [\mathbf{F}(c)]^{\mathsf{T}} \in \mathbb{R}^{N\times T}$, $\forall c \in C$ be the data matrix of $N = |C|$ (where $|\cdot|$ is the cardinality of a set) feature vectors with dimensionality T. $\mathbf{F}(c)$ represents the features assigned to a given voxel, c. In our case, $\mathbf{F}(c)$ contains the assigned signal intensity values at every voxel $c \in C$ at each time point $t \in \{0, 1, 2, \ldots, T-1\}$, where T is the number of time points in the DCE-MRI time series. $t = 0$ refers to the time at which the precontrast image is acquired and $t \in \{1, \ldots, T-1\}$ refer to the times at which the subsequent postcontrast images are acquired. The aim of SE is to reduce $\mathcal{F} \in \mathbb{R}^{N\times T}$ to a lower d-dimensional space where $d \ll T$. The three eigenvectors associated with the three smallest eigenvalues (i.e., $d = 3$ in this implementation of SE) at each voxel location in the image that result from the SE are used to represent the color values in the parametric eigenvector image (PrEIm). To implement this, the three selected eigenvector values are assigned to each of the three color channels [i.e., the first eigenvector value in the hue channel, the second eigenvector value in the saturation channel, and the third eigenvector in the value channel of a hue, saturation, value (HSV) image, see Fig. 1(b)].

Step 2. Calculate spatial gradients on the PrEIm: The spatial (X- and Y-directional) tensor-based gradients are derived from the SE eigenvectors, which are incorporated into the energy functional of a hybrid AC model. Tensor gradients derived from the vectorial image provide stronger gradients for driving the AC model than the corresponding gradient derived from a scalar image.[15]

Step 3. Manual initialization of the AC model: A point within the OOI is selected manually, which serves as the initialization for the AC model.

Step 4. Evolve AC on PrEIm: The hybrid AC deviates from traditional boundary- or region-based AC models by combining both boundary and region information from the image, allowing the two types of image information to simultaneously drive the AC model to optimize the curve such that: (1) the difference between region statistics inside and outside the AC is maximized; and (2) the gradient magnitude is maximized at the border between foreground and background areas of the image scene. Moreover, we employ a selective, intelligent weighting of the region, and boundary terms of the hybrid AC. This is done by identifying the optimal combination of weights for the region and boundary terms in the hybrid AC model.

IV. GRADIENT TENSORS IN SPECTRAL EMBEDDING SPACE

IV.A. Review of theory of spectral embedding

Let $\mathbf{v}(c)$ be the function that defines the eigenvectors associated with c, $\forall c \in C$, and let $\mathcal{V}$ be the eigenspace defined by $\mathbf{v}(C)$. For simplicity of notation in the SE formulation, we define $\mathbf{f}$ as a single vector in $\mathcal{F}$, dissociated from its spatial voxel location in the image and $\hat{\mathbf{v}} = [\mathbf{v}(c)\forall c \in C]^{\mathsf{T}} \in \mathbb{R}^{N\times d}$, as the vectorized form of $\mathbf{v}(c)$. The optimal $\hat{\mathbf{v}}$ is obtained by solving the generalized eigenvalue decomposition problem,

$$(\mathbf{D} - W)\hat{\mathbf{v}} = \hat{\mathbf{v}}\Lambda_d\mathbf{D}, \tag{1}$$

where Λ_d is the matrix corresponding to the eigenvalues associated with the smallest d eigenvectors. W is the weighted adjacency matrix that characterizes the similarity between pairwise observations, i and j. The graph edge weight of two nodes, i and j, can be formulated by the Gaussian similarity function $w(i, j) = \exp(\frac{-\|\mathbf{f}(i)-\mathbf{f}(j)\|_2^2}{\sigma_C^2})$, where σ_C is a scaling parameter. $\mathbf{D}$ is the degree matrix such that the degree of a vertex is defined as $\mathbf{d}_i = \sum_j w(i, j), i, j \in \{1, \ldots, N\}$. The graph theoretic derivation of the eigenvalue problem found in Eq. (1) can be found in Shi *et al.*[30] and von Luxburg.[33]

The resulting d eigenvectors corresponding to the d smallest eigenvalues at every voxel location in the image can be used to construct PrEIm representations of the DCE-MRI data (Fig. 1). Objects that are adjacent to each other in the embedding space will consequently have a similar color [Fig. 1(b)].

IV.B. Computing spatial gradients in spectrally embedded space

Following the calculation of the eigenvectors by solving the minimization of Eq. (1), the gradients of the embedding vectors can be calculated along the spatial coordinates axes, resulting in a tensor gradient function,$\nabla\mathcal{V}$.

$\nabla\mathcal{V}$ is inspired by the Cumani operator,[34] a second-order differential operator for vectorial images, based on the Di Zenzo multivalued geometry.[35] Thus, $\nabla\mathcal{V}$ defines a tensor gradient over the eigenvector space and the gradient is calculated via the local structure tensor.

For an eigenimage $\mathcal{V} = \mathbf{v}(C)$, where $\mathbf{v}(C)$, $\forall c \in C$, is the associated set of eigenvectors for the entire voxel scene, C, the L_2 norm of $\mathbf{v}(c)$ at each $c \in C$ can be written in matrix form as

$$d\mathbf{v}(c)^2 = \begin{bmatrix} dx \\ dy \end{bmatrix}^T \begin{bmatrix} \rho_{11} & \rho_{12} \\ \rho_{21} & \rho_{22} \end{bmatrix} \begin{bmatrix} dx \\ dy \end{bmatrix}, \tag{2}$$

where

$$\rho_{11} = \left(\frac{\partial \mathbf{v}(c)}{\partial x}\right)^T \left(\frac{\partial \mathbf{v}(c)}{\partial x}\right) = \left(\frac{\partial v_1(c)}{\partial x}\right)^2 + \left(\frac{\partial v_2(c)}{\partial x}\right)^2 + \left(\frac{\partial v_3(c)}{\partial x}\right)^2,$$

$$\rho_{12} = \rho_{21} = \left(\frac{\partial \mathbf{v}(c)}{\partial x}\right)^T \left(\frac{\partial \mathbf{v}(c)}{\partial y}\right) = \frac{\partial v_1(c)}{\partial x} \cdot \frac{\partial v_1(c)}{\partial y} + \frac{\partial v_2(c)}{\partial x} \cdot \frac{\partial v_2(c)}{\partial y} + \frac{\partial v_3(c)}{\partial x} \cdot \frac{\partial v_3(c)}{\partial y}. \quad (3)$$

Here, ρ_{22} is defined similar to ρ_{11} along the Y axis. It is important to note that ρ_{11}, ρ_{12}, and ρ_{22} are computed on the eigenvectors of each voxel in the embedding space. The matrix $\rho(\mathbf{v}(c)) = [\begin{smallmatrix}\rho_{11} & \rho_{12}\\ \rho_{21} & \rho_{22}\end{smallmatrix}]$ is the first fundamental form in vector eigenspace and is also referred to as the local structure tensor. For the matrix $[\rho(\mathbf{v}(c))]$, the maximum and minimum eigenvalues of the matrix ($\tilde{\lambda}_+$ and $\tilde{\lambda}_-$) represent the extreme rates of change in the direction of their corresponding eigenvectors. $\tilde{\lambda}_+$ and $\tilde{\lambda}_-$ may be formally expressed by $\tilde{\lambda}_\pm = (\rho_{11} + \rho_{22} \pm \sqrt{\triangle})/2$, where $\triangle = (\rho_{11} - \rho_{22})^2 + 4\rho_{12}^2$. The tensor gradient is defined as[12]

$$\gamma(\mathbf{v}(c)) = \sqrt{\tilde{\lambda}_+ - \tilde{\lambda}_-}, \quad (4)$$

$\forall c \in C$. Thus, $\nabla \mathcal{V} \approx \gamma(\mathbf{v}(C))$ when the tensor gradient is calculated over the entire image scene, C. From Eqs. (2)–(4), it is also easy to show that for voxel c the grayscale gradient $\sqrt{\frac{\partial^2 v_j}{\partial x^2} + \frac{\partial^2 v_j}{\partial y^2}}$, where $j = 1$, (widely employed for edge detection) is a special case of the tensor gradient $\gamma(\cdot)$. In contrast, the tensor gradient of the embedding vectors (v_1, v_2, v_3) in the XY plane are computed as described in Eq. (4). An example of the improved gradient information found in the tensor gradient derived from SE compared to the grayscale intensity image is shown in Fig. 3.

V. SPECTRAL EMBEDDING BASED ACTIVE CONTOUR

V.A. Active contour model and its energy functional

We assume that the image plane $\Omega \in \mathbb{R}^2$ is partitioned into two regions by a curve Υ. The foreground region, or region of interest (ROI), is defined as Ω_1, and the background region (i.e., the remainder of the image) is defined as Ω_2 (see Table I for further details). The relationship among Ω and its constituents are as follows:

$$\Omega = \Omega_1 \cup \Omega_2 \cup \Upsilon, \quad (5)$$

where Ω_1 and Ω_2 are nonoverlapping. In other words,

$$\Omega_1 \cap \Omega_2 = \emptyset. \quad (6)$$

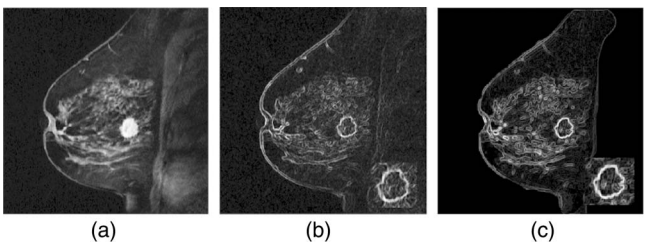

FIG. 3. (a) Original grayscale MR image of a malignant breast lesion at peak contrast enhancement along with the (b) grayscale gradient derived from PeakCE image and the (c) tensor gradient derived from PrEIm (not shown). Details of the lesion region are shown at the bottom right corner of (b) and (c). Note that the edges of the lesion in (c) are much stronger than those shown in (b), in turn generating a stronger edge based stopping criterion for SEAC.

V.B. Edge-based active contour

Previous AC methods have proposed various approaches to formulate the optimal partition of the image plane Ω, which can be obtained by the minimization of an energy functional. An AC deforms in order to approximate the border between regions of interest and noninterest.[11,13–15,36] In the simplified case, the energy functional is formulated as the integral of an edge detector function[10]

$$E_1 = \int_\Upsilon g(\mathbf{v}(c))dc, \quad (7)$$

where

$$g(\mathbf{v}(c)) = \frac{1}{1 + \gamma(\mathbf{v}(c))}. \quad (8)$$

Equation (7) will converge to the contour that represents the regions of steepest gradient in the image. Note that in this case the gradient function, $\gamma(\mathbf{v}(c))$ is often calculated by the gray level gradient.[36] However, in this paper we have chosen the gradient function to be a tensor gradient function.[15]

In order to maintain stable curve evolution and eliminate the need for reinitialization of the curve at each iteration of the evolution of the curve,[37] we have also chosen to implement a second term

$$E_2 = \int_\Omega \frac{1}{2}(\|\nabla\phi\|) - 1)^2 dc. \quad (9)$$

The combined energy functional is defined as

$$E^{\text{Bound}}(\phi) = \beta E_1 + \zeta E_2 = \beta \int_\Upsilon g(\mathbf{v}(c))dc + \zeta \int_\Omega \frac{1}{2}(\|\nabla\phi\|) - 1)^2 dc. \quad (10)$$

V.C. Region-based active contour

The region-based model employs statistical information derived from different regions (foreground and background) to drive the AC model, which is independent of the edge detector function and does not require precise initialization.[38] One important region-based AC model is the Rousson-Deriche model,[14] which assumes that the image plane comprises two regions and the intensities of voxels within each region satisfy a Gaussian distribution. The contour evolves as a result of competition between the log probability of current voxels c belonging to the foreground and background regions. The optimal image partition is generated by maximizing the *a posteriori* partition probability, $P(\Omega|\mathbf{v}(c))$. The assumptions are: (1) All partitions are equally possible.

(2) Homogeneity of a region exists within a given boundary. (3) Voxels within a given region are independent. The generalized energy functional for the region-based term can then be described as follows:[14]

$$E^{\text{Reg}}(\phi) = -\alpha_1 \int_\Omega [H(\phi)\log p(\mathbf{v}(c)|\theta_1) + (1-H(\phi))\log p(\mathbf{v}(c)|\theta_2)]dc + \alpha_2 \int_\Omega |\nabla H(\phi)|dc, \quad (11)$$

where $H(\phi)$ is the Heaviside function and $p(\mathbf{v}(c)|\theta_h)$ ($h \in \{1, 2\}$) is the multivariate Gaussian distribution function with parameter $\theta_h = \{\mu_h, \Sigma_h\}$, where μ_h and Σ_h are the mean and covariance of the intensity in the region $h(h \in \{1, 2\})$ and are estimated by

$$\mu_h = \frac{1}{|\Omega_h|}\int_{\Omega_h} \mathbf{v}(c)dc,$$

$$\Sigma_h = \frac{1}{|\Omega_h|}\int_{\Omega_h} (\mathbf{v}(c)-\mu_h)(\mathbf{v}(c)-\mu_h)^T dc. \quad (12)$$

V.D. Hybrid active contour energy functional

Since region-based AC models do not typically include boundary information, a hybrid AC model can be employed to combine the strengths of boundary-based (10) and region-based (11) models by incorporating both gradient and region information into the AC model. The corresponding energy functional can be shown as

$$E^{\text{Hybrid}}(\phi) = -\alpha \int_\Omega [H(\phi)\log p(\mathbf{v}(c)|\theta_1) + (1-H(\phi))\log p(\mathbf{v}(c)|\theta_2)]dc + \beta \int_\Omega g(\mathbf{v}(c))|\nabla H(\phi)|dc + \zeta \int_\Omega \frac{1}{2}(\|\nabla\phi\|)-1)^2 dc. \quad (13)$$

Using calculus of variations, the curve evolution function can be derived by minimizing the energy function (13),

$$\begin{cases} \dfrac{\partial\phi(t;c)}{\partial t} = \alpha\delta(\phi)[\log p(\mathbf{v}(c)|\theta_1) - \log p(\mathbf{v}(c)|\theta_2)] \\ \qquad + \beta\delta(\phi)\mathbf{div}\left[g(\mathbf{v}(c))\dfrac{\nabla\phi}{|\nabla\phi|}\right] \\ \qquad + \zeta\left[\Delta\phi - \mathbf{div}\left(\dfrac{\nabla\phi}{\|\nabla\phi\|}\right)\right], \\ \phi(0,c) = \phi_0(c), \quad \forall c \in \Upsilon, \end{cases} \quad (14)$$

where $H(\phi)$ is the Heaviside function, Ω_1 and Ω_2 are the image foreground and background, respectively, $\phi(t; c)$ is the level set function, α and β are positive constant parameters that can be used to variably weight the region- and boundary-based terms, ζ is the weight of the contour stabilization term [see Eq. (9)], and $\delta(\phi)$ is the Delta function. From an initial contour ϕ_0, the curve evolution function in Eq. (14) is evolved until model convergence. The iterative implementation of the curve evolution can be found in Sec. V.E.

V.E. SEAC algorithm

Input. $\hat{\mathcal{C}} = (C, \gamma)$
Output. Final AC: ϕ_T
begin
1. {Compute tensor gradient of PrEIm as described in Eqs. (2)–(4)}.
2. Calculate $g(\mathbf{v}(c)) = \frac{1}{1+\gamma(\mathbf{v}(c))}$;
3. Model $p(\mathbf{v}(c)|\theta_h)$, $h \in \{1, 2\}$ using multivariate Gaussians to approximate intensity distributions;
4. Formulate energy functional [Eq. (5)] using $p(\mathbf{v}(c)|\theta_h)$, $h \in \{1, 2\}$ and $g(\mathbf{v}(c))$;
5. Initialize $\phi(t; c) = \phi_0$, where $t = 0$;
6. **while** $|\phi(t; c) - \phi(t-1; c)| > \epsilon$ **do**
7. Compute $\frac{\partial\phi}{\partial t}$ [see Eq. (14)];
8. $t = t + 1$;
9. $\phi_T = \phi(t; c)$;
10. **end while**
end

VI. EXPERIMENTAL DESIGN

VI.A. Data description

A total of 50 (30 malignant, 20 benign) breast DCE-MRI studies were obtained from the Hospital at the University of Pennsylvania. All of these were clinical cases where a screening mammogram revealed a lesion suspicious for malignancy. All studies were collected under Institutional Review Board approval, and lesion diagnosis was confirmed by biopsy and histological examination. Sagittal T1-weighted, spoiled

TABLE I. Commonly employed notation and symbols.

Symbol	Description	Symbol	Description
C	2D Cartesian grid of voxels $c = (x, y)$	$\mathcal{C}$	2D image scene
$\mathbf{F}(c)$	Signal intensity vector of c	$\mathcal{F}$	Set of all time intensity vectors $[\mathbf{F}(c)]^{\mathsf{T}}, \forall c \in C$
$\mathbf{v}(c)$	Eigenvectors associated with voxel c	$\rho(\mathbf{v}(c))$	Local structure tensor of $\mathbf{v}(c)$
$\mathbf{f}$	Single feature vector	$\mathcal{V}$	Eigenscene associated with $\mathcal{C}$
$\mathbb{C}$	The zero level set $\mathbb{C} = \{c \in \Theta : \phi(c) = 0\}$	$\gamma(\mathbf{v}(c))$	Tensor gradient computed on $\mathbf{v}$
$H(\phi)$	Heaviside function $H(\phi) = \begin{cases} 1, & \phi(c) \geq 0; \\ 0, & \phi(c) < 0. \end{cases}$	$\Omega_h, h \in \{1, 2\}$	Region membership $\Omega_h = \begin{cases} \Omega_1, & \phi(c) \geq 0; \\ \Omega_2, & \phi(c) < 0. \end{cases}$
$\delta(\phi)$	Delta function: $\delta(\phi) = 0, \phi(c) \neq 0$; $\int_{\infty}^{\infty} \delta(\phi) d\phi = 1$. (Ref. 48)	$\phi(t; c)$	The level set function

gradient echo sequences with fat suppression consisting of one series before contrast injection of Gd-DTPA (precontrast) and three to eight series after contrast injection (postcontrast) were acquired at 1.5 T (Siemens Magnetom). Single slice dimensions were 384 × 384 or 512 × 512 with a slice thickness of 3 mm. Temporal resolution between postcontrast acquisitions was a minimum of 90 s.

VI.B. Implementation of SEAC

For each voxel, c, in each image, a dynamic signal intensity vector was created consisting of the signal intensity values of the voxel at each time point in the time series as described in Table I. For each dataset, a seed point is selected in the region of interest based on visual inspection of the MR image. The same seed point is used across all alternative image representations. In order to ensure the fidelity of manual seed point selection, we also performed an experiment where 20 random seed points were selected for curve evolution on each dataset and calculated the standard deviation from the mean dice similarity coefficient for each lesion. The average standard deviation for 20 randomly selected seed points over all 50 lesions was 0.098.

Since the hybrid active contour incorporates region and boundary information, the individual constituent terms need to be differentially weighted based on the specific image domain to optimize the active contour. Thus, we performed a brute force examination of these weights by first trying all combinations of weights on all the datasets. The accuracy of the segmentation as described in Sec. VI.C was used to determine the optimal parameters for a given image initialization. The range of parameters used with each AC model is described in Table II, and these values were based on the empirically derived optimal weights used previously.[40] The stopping criterion for the AC is that which minimizes the energy function such that the difference in energy between a given iteration of the AC and the iteration preceding it is less than a predefined threshold (see Sec. V.E for further details). The best results for the SEAC hybrid model were a combination of weighting the region term at 0.4 and the boundary term at 6.4 and weighting the region term at 0.1 and the boundary term at 6.4. The best results for the PCA weighted the region term at 0.2 and the boundary term at 6.4.

VI.C. Comparative image representation strategies

Like SE, FCM, and PCA are applied to the images on a per-voxel basis that allows for direct comparison of the methods to serve as an initialization to the AC model.

VI.C.1. Fuzzy c-means

Fuzzy c-means clustering as described in Chen *et al.*[6] is a popular scheme for automated segmentation of breast lesions on DCE-MRI.[41,42] FCM is a data clustering scheme similar to k-means in that data are clustered around a prescribed number of centroids. However, unlike k-means, the resulting class membership is a fuzzy membership to each cluster. We implement FCM similar to the method in Shi *et al.*[8] (referred to as FCM+AC) to compare the AC driven by FCM to that driven by SE in SEAC, where FCM is applied to the time-intensity vectors, $\mathcal{F}$.

VI.C.2. Principal component analysis

PCA (Ref. 43) is a linear dimensionality reduction method which attempts to reduce the dimensionality of the data while

TABLE II. Summary of experiments and corresponding parameters.

Method	Comparison strategies ($n = 50$)	Parameters used
Boundary	PeakCE, PCA, FCM, PrEIm	$\alpha = 0, \beta = 1, \zeta = 1$
Region	PeakCE, PCA, FCM, PrEIm	$\alpha = 1, \beta = 0, \zeta = 1$
Hybrid	FCM, PrEIm	$\alpha, \beta \in \{0.1, 0.2, 0.4, 0.8, 1.6, 3.2, 6.4, 12.8\}$, $\zeta = 1$
SVM classification	FCM, PrEIm	Radial basis function (Ref. 39)

retaining maximum variance of the dataset. PCA is most popularly implemented by performing an eigenvalue decomposition of a covariance matrix generated from the original data. The resulting eigenvectors are then considered to be the principal components, and the first few retain the maximum variance in the original dataset. In addition, if the eigenvectors are chosen to be orthonormal, then the variance captured by a given eigenvector is reflected by the corresponding eigenvalue. In this study, the input matrix to PCA is also $\mathcal{F}$.

VI.C.3. Applying the hybrid active contour to the comparative strategies

After FCM and PCA are performed on all images, the hybrid active contour model is applied to both the three-dimensional FCM parametric image result (referred to as FCM+AC), which uses three class probability clusters, and the three-dimensional PCA parametric image result (referred to as PCA+AC), which uses three eigenvectors at each pixel location. In order to demonstrate the limitations of using the grayscale intensity images, we also compare SEAC to an AC driven by the PeakCE image.

VI.C.4. Segmentation performance evaluation measures

VI.C.4.a. Ground truth generation. The ROI associated with the lesion was manually segmented via MRIcro imaging software[44] by an attending radiologist with expertise in MR mammography who was naive to the lesion diagnosis. The radiologist selected a 2D slice of the MRI volume that was most representative of each lesion, and the analyses were performed only for that 2D slice. The ground truth segmentation is defined as the manual segmentation performed by the radiologist, and ground truth diagnosis was confirmed on histopathologic examination of lesion biopsy by a pathologist.

VI.C.4.b. Boundary-based metrics. Mean absolute difference (MAD) is calculated by evaluating the mean difference between each point, c_z, on $G_1^a(\hat{\mathcal{C}}) = \{c_z | z \in \{1, \ldots, Z\}\}$ (SEAC, PCA+AC or FCM+AC), where $Z = |G_1^a(\hat{\mathcal{C}})|$ and $|\cdot|$ is the cardinality of any set, and the corresponding closest point, c_ψ, on the ground truth (GT) manual segmentation $G_1^b(\mathcal{C}) = \{c_\psi | \psi \in \{1, \ldots, |G_1^b(\mathcal{C})|\}$ such that,

$$\mathrm{MAD} = \frac{1}{Z}\sum_{z=1}^{Z}[\min_{\psi} \|c_z - c_\psi\|_2]. \tag{15}$$

Lower values of MAD reflect a more similar segmentation to the GT manual segmentation.

We also calculate maximum Hausdorff distance ($\mathrm{HD}_{\max}$), which is calculated as

$$\mathrm{HD}_{\max} = \max_{z}[\min_{\psi} \|c_z - c_\psi\|_2] \tag{16}$$

and reflects the maximum error between the automated and manual segmentations.

VI.C.4.c. Area-based metrics. Dice similarity coefficient (DSC) is calculated as follows:

$$\mathrm{DSC} = \frac{2\left|G_2^a(\hat{\mathcal{C}}) \cap G_2^b(\mathcal{C})\right|}{\left|G_2^a(\hat{\mathcal{C}})\right| + \left|G_2^b(\mathcal{C})\right|}, \tag{17}$$

where $G_2^a(\hat{\mathcal{C}})$ is the area enclosed by the automated segmentation and $G_2^b(\mathcal{C})$ is the area enclosed by the manual GT segmentation. The closer the DSC value is to 1, the more similar the automated lesion segmentation is to the GT segmentation.

VI.C.4.d. Classifier-based metrics. Because an accurate lesion segmentation is necessary for accurate morphological feature extraction,[1,2] classification accuracy would be a way to test SEAC's ability to function in the setting of a computer aided diagnosis system compared to other state of the art breast lesion segmentation methods. Morphological features[45] (area overlap ratio, normalized average radial distance ratio, standard deviation of normalized distance ratio, variance of distance ratio, compactness, and smoothness) based on the lesion contour are extracted and used in conjunction with a support vector machine (SVM) classifier to determine if morphological features based on SEAC segmentations will result in higher classifier accuracy compared to morphological features based on FCM+AC or PCA+AC segmentations of breast lesions. We calculated six morphological features[45] on 50 datasets (20 benign; 30 malignant).

The boundaries resulting from SEAC, FCM+AC, and PCA+AC were used for morphological feature extraction. The features, which are obtained for each lesion via each of the different segmentation schemes (SEAC, FCM+AC, PCA+AC), were then used in conjunction with a SVM classifier[39] with ten trials of tenfold cross validation to determine the lesion diagnosis. The distance of an object from the hyperplane was then converted to a pseudolikelihood[45] which was used to generate a ROC curve for evaluating the different SVM classifiers.

VI.C.4.e. Paired t-test. For the optimized hybrid AC model, statistical analysis is performed by calculating a paired t-test[6] between the metrics obtained using FCM+AC and PCA+AC compared to SEAC. For the classification experiment, a population mean of 0.5 was used since the AUC of each method is being compared to an AUC of 0.5.[42]

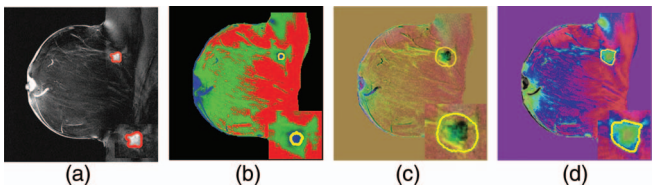

FIG. 4. (a) Ground truth segmentation of the lesion and alternative image representations using (b) FCM, (c) PCA, and (d) SEAC. Similar colors in each of figures (b)–(d) demonstrate voxels taken to have similar enhancement curves by the respective algorithm. The inset at the bottom right of each figure (b)–(d) demonstrates the final segmentation (yellow contour) using a boundary-based AC model. (d) SEAC provides the final contour most similar to (a) ground truth segmentation since (b) FCM+AC under-segments the lesion and (c) PCA+AC overshoots the boundary of the lesion.

TABLE III. Evaluation of image representations in conjunction with a boundary-based AC ($n = 50$).

AC method	MAD ($\mu \pm \sigma$ pixels)	DSC ($\mu \pm \sigma$)	HD_{max} ($\mu \pm \sigma$ pixels)
PeakCE + AC	7.26 ± 12.02	0.56 ± 0.31	13.11 ± 14.11
FCM + AC	6.64 ± 6.37	0.50 ± 0.32	11.86 ± 10.14
PCA + AC	5.50 ± 4.23	0.52 ± 0.25	11.2 ± 7.50
SEAC	5.87 ± 5.94	0.57 ± 0.30	11.06 ± 9.90

TABLE IV. Evaluation of image representations in conjunction with a region-based AC ($n = 50$). (PeakCE+AC and FCM+AC results omitted due to instability of the respective region-based ACs.)

AC method	MAD ($\mu \pm \sigma$)	DSC ($\mu \pm \sigma$)	HD_{max} ($\mu \pm \sigma$)
PCA + AC	4.87 ± 4.35	0.48 ± 0.24	10.9 ± 7.01
SEAC	4.24 ± 3.80	0.53 ± 0.26	9.76 ± 7.35

VII. EXPERIMENTAL RESULTS AND DISCUSSION

In this study, we evaluate two different aspects of SEAC. (1) We compare the alternative data representations obtained via peakCE, FCM, PCA, and SE in terms of their ability to drive region-based and boundary-based AC segmentation schemes. We hypothesize that SE will provide better boundary and region statistics for driving an AC segmentation scheme than peakCE, FCM, or PCA. (2) We compare the FCM+AC and PCA+AC schemes with SEAC with respect to the ability of each to drive a hybrid AC model.

VII.A. Comparison of different image representation schemes in capturing gradients

Figure 4 shows an example of a boundary-based AC driven by FCM, PCA, and SEAC. In this example, it is clear that the SE image would provide better gradient information for driving a boundary-based AC. For the particular study considered, the AC was unable to detect any strong boundaries using the FCM image, and therefore the AC did not evolve much beyond the manual initialization. Table III shows the boundary- and area-based measures of using a boundary-based AC alone with FCM+AC, PCA+AC, and SEAC. The boundary-based AC performed best with SEAC in terms of DSC and HD_{max}. PCA performed slightly better than SEAC in terms of MAD.

VII.B. Comparison of different image representation schemes in capturing region statistics

Figure 5 shows a region-based AC model driven by PeakCE, FCM, PCA, and SE. PeakCE and FCM performed particularly poorly in conjunction with the region-based AC. The PeakCE and FCM initializations were unable to produce a stable curve evolution based solely on region statistics, and thus, no results are reported for PeakCE+AC or FCM+AC in Table IV. Table IV shows the performance of a region-based AC in terms of MAD, DSC, and HD_{max} for SE and PCA. Again, SEAC provided the segmentations that were most similar to ground truth in terms of MAD, DSC, and HD_{max}. Considering the fact that dimensionality reduction methods are meant to preserve global patterns in the data, it is not surprising that the region term is able to capitalize on this strength of both the linear and NLDR methods used in this paper.

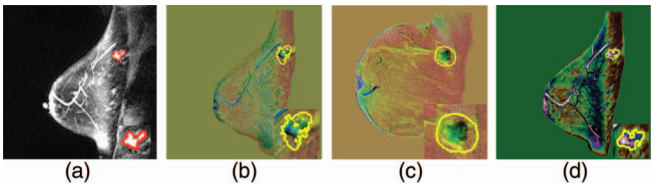

FIG. 5. (a) Ground truth segmentation and alternative image representations using (b) FCM, (c) PCA, and (d) SEAC. Similar colors in each of figures (b)−(d) demonstrate voxels taken to have similar enhancement curves by the respective algorithm. The inset at the bottom right of each figure (b)−(d) demonstrates the final segmentation (yellow contour) using a region-based AC model. Note that FCM produced no final contour (b).

VII.C. Comparing image segmentation strategies

VII.C.1. Boundary-based measures

We compare SEAC to a version of the previously published[8] FCM+AC model as well as PCA+AC using a hybrid active contour model. Table V shows the results for the optimized hybrid models for PCA+AC, FCM+AC, and SEAC. SEAC and PCA+AC resulted in a statistically significant improvement over FCM+AC in terms of MAD, DSC, and HD_{max} (indicated by an asterisk (*) in Table V). Since the FCM segmentations degraded when the region-based term was added to the model, the optimized SEAC and PCA+AC models are compared to the boundary-based FCM+AC. In addition, a *t*-test was performed to test the hypothesis that (1) SEAC more accurately approximates the ground truth segmentation in terms of MAD, HD, and DSC compared to FCM; and (2) SEAC demonstrates a statistically significant improvement segmentation over the popular FCM segmentation method. Figure 6 shows an example of the hybrid AC segmentation driven by FCM, PCA, and SE, which shows the improved segmentation using SEAC compared to FCM+AC and PCA+AC.

VII.C.2. Classifier accuracy

Once the AC was optimized for FCM+AC, PCA+AC, and SEAC, the best case active contour for each segmentation

TABLE V. Evaluation of image representations in conjunction with a hybrid AC ($n = 50$, $^*p < 0.05$).

AC method	MAD ($\mu \pm \sigma$)	DSC ($\mu \pm \sigma$)	HD_{max} ($\mu \pm \sigma$)
FCM + AC	6.64 ± 6.37	0.50 ± 0.32	11.86 ± 10.14
PCA + AC	*3.11 ± 3.09	*0.73 ± 0.22	8.17 ± 7.36
SEAC	*2.31 ± 2.26	*0.74 ± 0.21	*5.64 ± 5.04

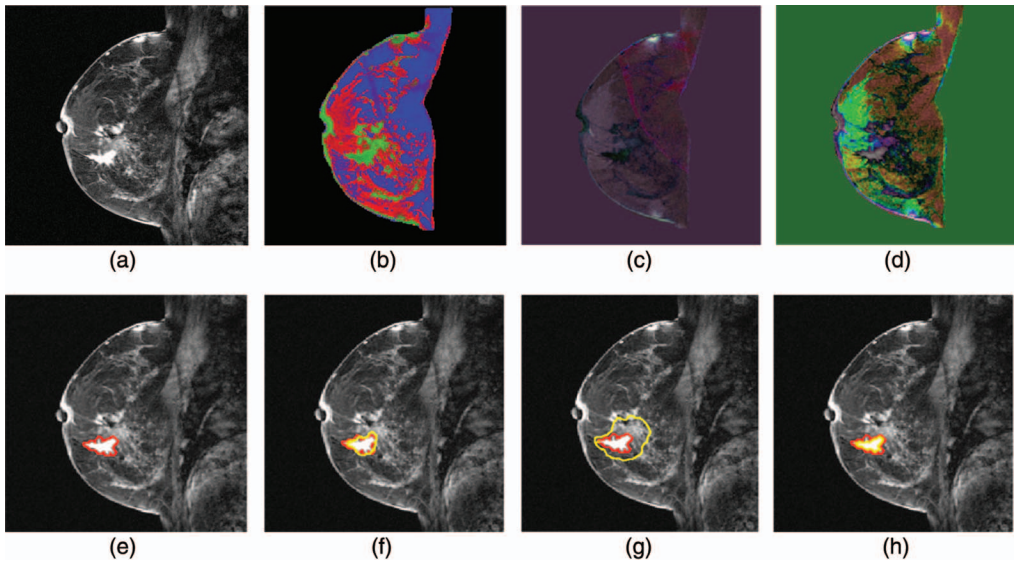

FIG. 6. (a) Original grayscale postcontrast image and image representations derived from (b) FCM, (c) PCA and (d) SE. Note that the colormaps displayed for the three methods only reflect the voxel similarities as determined by the three schemes, voxels with similar time-intensity curves being assigned similar colors. The second row of images shows the ground truth segmentation (e) in red and the hybrid AC segmentation (yellow line) overlaid on ground truth driven by (f) the FCM+AC segmentation, (g) PCA+AC segmentation, and (h) SEAC.

method was used to generate the lesion contours from which morphological features are extracted. Lesion classification was then performed using a SVM classifier[39] based on these automatically derived contours. The classification results using the automatically derived contours are then compared to classification driven by contours from manual segmentations. A Student's *t*-test is then performed to compare the AUC for each classifier to the null hypothesis, which is an AUC = 0.5, or no difference in classification from that expected by chance.[42] This is tested against the hypothesis that there is no statistical difference between the AUC derived from breast lesion classification using the SEAC, PCA, or FCM segmentations and an AUC of 0.5. Table VI shows the SVM classification AUC for ten trials of tenfold cross validation based on morphological features based on FCM+AC and SEAC. SEAC performed better than FCM+AC and PCA+AC, and the AUC for the ROC curve for SEAC is statistically significant compared to an AUC of 0.5,[42] whereas the AUCs for FCM+AC and PCA+AC was not statistically significantly better than an AUC of 0.5. The AUC of 0.67 for SEAC is also comparable to the AUC for lesion diagnosis based on morphological features found elsewhere in the literature.[46] These results suggest that SEAC was capable of capturing subtleties of lesion morphology that are critical to accurate lesion classification.

TABLE VI. Classification accuracy based on automated segmentation ($n = 50$, $^* p < 0.05$).

Segmentation method	AUC ($\mu \pm \sigma$)
FCM + AC	0.50 ± 0.07
PCA + AC	0.49 ± 0.07
SEAC*	0.67 ± 0.05

VIII. CONCLUDING REMARKS

In this paper, we demonstrate that the spectral embedding based active contour (SEAC): (1) provides a better image representation for both boundary- and region-based AC segmentation schemes compared to PeakCE+AC, FCM+AC, or PCA+AC; (2) provides a better image representation for a hybrid active contour model than FCM, a popular segmentation method for breast DCE-MRI; and (3) provides a more accurate classification of breast lesions based on quantitative morphologic features as captured on DCE-MRI.

We have presented a new AC model [spectral embedding based AC, (SEAC)] involving use of an alternative image representation obtained via a nonlinear dimensionality reduction scheme that results in stronger boundary gradients and improved region statistics, in turn providing improved stopping criteria for the AC. SE transforms the high-dimensional DCE-MRI time series data to a reduced dimensional space that is composed of an orthogonal basis set of eigenvectors. This transformed space provides strong tensor gradients and improved region statistics compared to those that might be obtained from the original grayscale image alone. On a cohort of 50 breast DCE-MRI studies, we showed that SEAC best approximated manual lesion segmentations when using both a boundary- and a region-based AC model when compared to the widely used FCM segmentation as well as PeakCE+AC and PCA+AC. We also demonstrated that on a cohort of 50 lesions, the morphological features derived from SEAC yielded better lesion classification compared to morphological features derived from a PCA- or FCM-based segmentation. While in this work, we demonstrate the use of SEAC with breast DCE-MRI data, SEAC could be easily applied to segmenting structures on other high-dimensional, time-series imaging data as well. However, it is important to note that, as with any information-based segmentation scheme, SEAC

is based on the theory that different tissues will have different uptake curves. Therefore, if two tissues have similar contrast uptake curves, they may be included in the same lesion segmentation, and this is a potential limitation of SEAC.

When using a hybrid AC model, determining the weights for each term in the energy functional is a difficult task. In this paper, the optimal weights for the hybrid AC model were obtained by first performing the segmentations using various combinations of a predetermined range of weights. In performing the experiments with hybrid active contour models, it was noted that while the PCA+AC model performed well with a heavily weighted boundary-based term, the SEAC method performed well for some datasets with a heavily weighted region term and for some datasets with a heavily weighted boundary term. The relative weights of the region and boundary terms could be predicted by the experiments which examined segmentation accuracy with the boundary and region terms alone. The weights that provided the best segmentations for the PCA+AC model used one set of weights, while SEAC performed best with two sets of weights. This flexibility of SEAC may, in fact, be one of the advantages of SEAC over PCA+AC, and this may make SEAC less susceptible to image artifacts. While this approach to the determination of weights did provide some improvement over both the boundary- and region-based AC models, it is quite possible that these weights are not fully optimized, and future work will be devoted to determining the best approach to this problem. Another area for future work relates to the bias field correction performed on the images using the N3 bias field correction method.[47] In this study, we found that bias field correction did not improve the accuracy of SEAC (see the Appendix). Although this should be further explored in future work, it seems as though the full dynamic range of image intensities is useful in generating the PrEIm. Our findings may also suggest that N3 is not the appropriate bias field correction scheme for this particular dataset.

The classification results demonstrated in this paper also suggest that endpoint classification may be an additionally important metric for the evaluation of automated segmentation methods designed for use in conjunction with computer-aided diagnosis systems.

We also found that for our datasets, which ranged in image grid size from 384 × 384 to 512 × 512 voxels, that total run-time ranged from approximately 3−12 min on a 72 GB RAM, 2.66 GHz, 2x Quad-Core Xeon X5550 processor machine, depending on the size of the image. Future work will also be devoted to optimizing SE and AC code components for run-time efficiency.

ACKNOWLEDGMENTS

This work was made possible by grants from the National Institute of Health (R01CA136535, R01CA140772, R43EB015199, R21CA167811), National Science Foundation (IIP-1248316), the QED award from the University City Science Center and Rutgers University, the New Jersey Commission on Cancer Research (Predoctoral Fellowship 09-2407-CCR-EO). We would also like to thank Mark Rosen, MD, PhD for his expert segmentations of the lesions.

APPENDIX: EFFECTS OF BIAS FIELD CORRECTION ON SEGMENTATION ACCURACY

In order to examine the effects of bias field correction on classification accuracy, we calculated SEAC before and after bias field correction. Bias field artifacts were corrected by means of the popular N3 algorithm,[47] which incrementally deconvolves smooth bias field estimates from acquired image data, resulting in a bias-field corrected image. We then used the same set of weights ($\alpha = 0.4$, $\beta = 6.4$) applied to both sets of PrEIm. The final results are listed in Table VII. In this study, we found that bias field correction did not improve the accuracy of SEAC. Although this should be further explored in future work, it seems as though the full dynamic range of image intensities is useful in generating the PrEIm. Our findings may also suggest that N3 is not the appropriate bias field correction scheme for this particular dataset.

TABLE VII. Segmentation accuracy in conjunction with bias field correction ($n = 50$).

Segmentation method	DSC ($\mu \pm \sigma$)
With bias field correction	0.57 ± 0.30
Without bias field correction	0.66 ± 0.22

[a]Electronic mail: agnersc@umdnj.edu
[b]Electronic mail: anant.madabhushi@case.edu

[1]D. M. Ikeda, N. Hylton, K. Kinkel, M. G. Hochman, C. Kuhl, W. A. Kaiser, J. C. Weinreb, S. F. Smazal, H. Degani, P. Viehweg, J. Barclay, and M. D. Schnall, "Development, standardization, and testing of a lexicon for reporting contrast-enhanced breast magnetic resonance imaging," J. Magn. Reson. Imaging **13**, 889–895 (2001).
[2]M. D. Schnall, J. Blume, D. A. Bleumke, G. A. DeAngelis, N. DeBruhl, S. Harms, S. H. Heywang-Kobrunner, N. Hylton, C. Kuhl, E. D. Pisano, P. Causer, S. J. Schnitt, D. Thickman, C. B. Stelling, P. T. Weatherall, C. Lehman, and C. A. Gastonis, "Diagnositc architectural and dynamic features at breast MR imaging: Multicenter study," Radiology **238**(1), 42–53 (2006).
[3]K. Kinkel, T. H. Helbich, L. J. Esserman, J. Barclay, E. Schwerin, E. A. Sickles, and N. M. Hylton, "Dynamic high-spatial-resolution MR imaging of suspicious breast lesion: Diagnostic criteria and interobserver variability," Am. J. Roentgenol. **175**(1), 35–43 (2000).
[4]B. K. Szabo, P. Aspelin, and M. K. Wiberg, "Neural network approach to the segmentation and classification of dynamic magnetic resonance images of the breast: Comparison with empiric and quantitative kinetic parameters," Acad. Radiol. **11**, 1344–1354 (2004).
[5]T. Twellmann, A. Meyer-Baese, O. Lange, S. Foo, and T. W. Nattkemper, "Model-free visualization of suspicious lesions in breast MRI based on supervised and unsupervised learning," Eng. Applic. Artif. Intell. **21**, 129–140 (2008).
[6]W. Chen, M. L. Giger, U. Bick, and G. M. Newstead, "Automatic identification and classification of characteristic kinetic curves of breast lesion on DCE-MRI," Med. Phys. **33**(8), 2878–2887 (2006).
[7]Q. Wu, M. Salganicoff, A. Krishnan, D. S. Fussell, and M. K. Markey, "Interactive lesion segmentation on dynamic contrast enhanced breast MRI using a Markov model," Proc. SPIE **6144**, 61444M (2006).
[8]J. Shi, B. Sahiner, H.-P. Chan, C. Paramagul, L. M. Hadjiiski, M. Helvie, and T. Chenevert, "Treatment response assessment of breast masses on dynamic contrast-enhanced magnetic resonance scans using fuzzy c-means clustering and level set segmentation," Med. Phys. **36**(11), 5052–5063 (2009).

[9]M. Kass, A. Witkin, and D. Terzopoulos, "Snakes: Active contour models," Int. J. Comput. Vis. **1**(4), 321–331 (1988).
[10]V. Caselles, R. Kimmel, and G. Sapiro, "Geodesic active contours," Int. J. Comput. Vis. **22**, 61–79 (1997).
[11]T. F. Chan and L. A. Vese, "Active contours without edges," IEEE Trans. Image Process. **10**(2), 266–277 (2001).
[12]G. Sapiro, "Color snakes," Comput. Vis. Image Underst. **68**(2), 247–253 (1997).
[13]T. F. Chan, B. Y. Sandberg, and L. A. Vese, "Active contours without edges for vector-valued images," J. Visual Commun. Image Represent **11**(2), 130–141 (2000).
[14]M. Rousson and R. Deriche, "A variational framework for active and adaptative segmentation of vector valued images," in *Proceedings of the Workshop on Motion and Video Computing, 2002*, Workshop occurred in Orlando, FL (IEEE Computer Society, Los Alamitos, CA, 2002), pp. 56–61.
[15]J. Xu, A. Janowczyk, S. Chandran, and A. Madabhushi, "A high-throughput active contour scheme for segmentation of histopathological imagery," Med. Image Anal. **15**(6), 851–862 (2011).
[16]W. G. Bradley and B. J. Glenn, "The effect of variation in slice thickness and interslice gap on MR lesion detection," AJNR Am. J. Neuroradiol. **8**(6), 1057–1062 (1987).
[17]G. H. Glover and N. J. Pelc, "Nonlinear partial volume artifacts in x-ray computed tomography," Med. Phys. **7**(3), 238–248 (1980).
[18]P. K. Saha and J. K. Udupa, "Scale-based diffusive image filtering preserving boundary sharpness and fine structures," IEEE Trans. Med. Imaging **20**(11), 1140–1155 (2001).
[19]L. G. Nyul, J. K. Udupa, and P. K. Saha, "Incorporating a measure of local scale in voxel-based 3-D image registration," IEEE Trans. Med. Imaging **22**(2), 228–237 (2003).
[20]P. K. Saha, J. K. Udupa, and D. Odhner, "Scale-based fuzzy connected image segmentation: Theory, algorithms, and validation," Comput. Vis. Image Underst. **77**(2), 145–174 (2000).
[21]P. K. Saha, "Tensor scale: A local morphometric parameter with applications to computer vision and image processing," Comput. Vis. Image Underst. **99**(3), 384–413 (2005).
[22]P. K. Saha, H. Zhang, J. K. Udupa, and J. C. Gee, "Tensor scale-based image registration," Proc. SPIE **5032**, 314–324 (2003).
[23]A. Madabhushi, J. K. Udupa, and A. Souza, "Generalized scale: Theory, algorithms, and application to image inhomogeneity correction," Comput. Vis. Image Underst. **101**(2), 100–121 (2006).
[24]A. Souza, J. K. Udupa, and A. Madabhushi, "Image filtering via generalized scale," Med. Image Anal. **12**(2), 87–98 (2008).
[25]A. Madabhushi and J. K. Udupa, "New methods of MR image intensity standardization via generalized scale," Med. Phys. **33**(9), 3426–3434 (2006).
[26]G. Hamarneh, C. McIntosh, and M. S. Drew, "Perception-based visualization of manifold-valued medical images using distance-preserving dimensionality reduction," IEEE Trans. Med. Imaging **30**(7), 1314–1327 (2011).
[27]E. Eyal, D. Badikhi, E. Furman-Haran, F. Kelcz, K. J. Kirshenbaum, and H. Degani, "Principal component analysis of breast DCE-MRI adjusted with a model-based method," J. Magn. Reson Imaging **30**(5), 989–998 (2009).
[28]A. R. Jamieson, M. L. Giger, K. Drukker, H. Li, Y. Yuan, and N. Bhooshan, "Exploring nonlinear feature space dimension reduction and data representation in breast CADx with Laplacian eigenmaps and t-SNE," Med. Phys. **37**(1), 339–351 (2010).
[29]G. Lee, C. Rodriguez, and A. Madabhushi, "Investigating the efficacy on nonlinear dimensionality reduction schemes in classifying gene and protein expression studies," IEEE/ACM Trans. Comput. Biol. Bioinf. **5**, 368–384 (2008).
[30]J. Shi and J. Malik, "Normalized cuts and image segmentation," IEEE Trans. Pattern Anal. Mach. Intell. **22**(8), 888–905 (2000).
[31]M. Meila and J. Shi, "A random walks view of spectral segmentation," In *Proceedings of the Tenth International Workshop on Artificial Intelligence and Statistics (AISTATS)*, Eighth International Workshop on Artificial Intelligence and Statistics. January 4–7, 2001, Key West, FL, 2001.
[32]Y. Weiss, "Segmentation using eigenvectors: A unifying view," IEEE Int. Conf. Comput. Vis. **2**, 975–982 (1999).
[33]U. von Luxburg, "A tutorial on spectral clustering," Techinical Report No. TR-149 (Max Planck Institute for Biological Cybernetics, 2006).
[34]A. Cumani, *Edge Detection in Multispectral Images* (Academic, New York, 1991), pp. 40–51.
[35]S. Di Zenzo, *A Note on the Gradient of a Multi-Image* (Academic, San Diego, CA, 1986), Vol. 33, pp. 116–125.
[36]L. D. Cohen, "On active contour models and balloons," Comput. Vis. Graph. Image Process. **53**(2), 211–218 (1991).
[37]C. Li, C. Xu, C. Gui, and M. D. Fox, "Level set evolution without re-initialization: A new variational formulation," in *Proceedings of the 2005 IEEE Computer Society Conference on Computer Vision and Pattern Recognition (CVPR'05)* (IEEE Computer Society, Washington, DC, 2005), Vol. 1, pp. 430–436.
[38]H. Fatakdawala, J. Xu, A. Basavanhally, G. Bhanot, S. Ganesan, M. Feldman, J. E. Tomaszewski, and A. Madabhushi, "Expectation maximization-driven geodesic active contour with overlap resolution (EMaGACOR): Application to lymphocyte segmentation on breast cancer histopathology," IEEE Trans. Biomed. Eng. **57**(7), 1676–1689 (2010).
[39]C. Cortes and V. Vapnik, "Support-vector networks," Mach. Learn. **20**(3), 273–297 (1995).
[40]S. C. Agner, J. Xu, M. Rosen, S. Karthigeyan, S. Englander, and A. Madabhushi, "Spectral embedding based active contour (SEAC): Application to breast lesion segmentation on DCE-MRI," Proc. SPIE **7963**, 796305 (2011).
[41]K. Nie, J.-H. Chen, H. J. Yu, Y. Chu, O. Nalcioglu, and M.-Y. Su, "Quantitative analysis of lesion morphology and texture features for diagnostic prediction in breast MRI," Acad. Radiol. **15**(12), 1513–1525 (2008).
[42]N. Bhooshan, M. L. Giger, S. A. Jansen, H. Li, L. Lan, and G. M. Newstead, "Cancerous breast lesions on dynamic contrast-enhanced MR images: Computerized characterization for image-based prognostic markers," Radiology **254**(3), 680–690 (2010).
[43]I. T. Jolliffe, *Principal Component Analysis*, Springer Series in Statistics, 2nd ed. (Springer-Verlag, New York, 2002).
[44]C. Rorden and M. Brett, "Stereotaxic display of brain lesions," Behav. Neurol. **12**(4), 191–200 (2000).
[45]S. C. Agner, S. Soman, E. Libfeld, M. McDonald, K. Thomas, S. Englander, M. A. Rosen, D. Chin, J. L. Nosher, and A. Madabhushi, "Textural kinetics: A novel dynamic contrast-enhanced (DCE)-MRI feature for breast lesion classification," J. Digit. Imaging **24**(3), 446–463 (2011).
[46]K. G. A. Gilhuijs, M. L. Giger, and U. Bick, "Computerized analysis of breast lesions in three dimensions using dynamic magnetic-resonance imaging," Med. Phys. **25**(9), 1647–1654 (1998).
[47]J. G. Sled, A. P. Zijdenbos, and A. C. Evans, "A nonparametric method for automatic correction of intensity nonuniformity in MRI data," IEEE Trans. Med. Imaging **17**(1), 87−97 (1998).
[48]H. J. Weber and G. B. Arfken, *Mathematical Methods for Physicists* (Academic, San Diego, 2003).